

Tectonic and glacial contributions to focused exhumation in the Olympic Mountains, Washington, USA

Lorenz Michel, Todd A. Ehlers *, Christoph Glotzbach, Byron A. Adams, Konstanze Stübner

Department of Geosciences, University of Tübingen, Tübingen, 72074, Germany

** Corresponding Author, todd.ehlers@uni-tuebingen.de*

DR1. ADDITIONAL BACKGROUND INFORMATION

The modern configuration of the Cascadia subduction zone formed during subduction of the Juan de Fuca plate beneath North America since the latest Eocene (Brandon and Vance, 1992). At present, the convergence rate between both plates reaches 34 km/Ma at the latitude of the Olympic Mountains (Dobrovine and Tarduno, 2008). The Olympic Mountains represent the aerially exposed part of the accretionary wedge (Tabor and Cady, 1978), whereas to the north beneath Vancouver Island and to the south beneath the Oregon Coast Range the wedge can only be found offshore (see Figure DR1a). A peculiar feature of the Cascadia subduction zone is a bend in the subducted slab beneath the Olympic Mountains (Figure DR1a). The wavelength of this bend and the resulting curvature of the slab differ, depending on which data set is used. Crosson and Owens (1987) provide a data set, where the wavelength is close to the size of the Olympics, whereas in a more recent model for slab geometry (Hayes et al., 2012; McCrory et al., 2012) the bend has a longer wavelength, so that the curved part of the slab also lies beneath the southern tip of Vancouver Island.

The Olympic Mountains consist of two tectono-stratigraphic units (see Figure DR1b), separated by a thrust fault (the Hurricane Ridge Fault, HRF): the Coast Range Terrain (CRT) and the Olympic Structural Complex (OSC). The CRT represents the upper plate and consists of Eocene aged basaltic rocks overlain and intercalated with sedimentary rocks of Eocene to Miocene age (Tabor and Cady, 1978; Eddy et al., 2017). The origin of these Eocene aged partly marine basaltic rocks is disputed (plume-derived plateau vs. back-arc volcanics), but recent studies suggest them to represent an oceanic plateau (Phillips et al., 2017; Eddy et al., 2017). For a full discussion on this point we refer the interested reader to Phillips et al. (2017). Contrary to that, the OSC dominantly consists of marine turbidite sequences or slate of Eocene to Miocene age and minor basaltic lenses, which are interpreted as the actual accretionary wedge (Tabor and Cady, 1978; Brandon et al., 1998). The OSC can be further divided in the three subunits coastal, upper and lower OSC (Brandon et al., 1998). Rocks with the youngest depositional ages (Miocene) can be found in the coastal OSC. In general, the metamorphic overprint of the rocks from the OSC is low, increases from west to east and the highest metamorphic overprint is found in the center of the range in the area neighboring the HRF (Tabor and Cady, 1978).

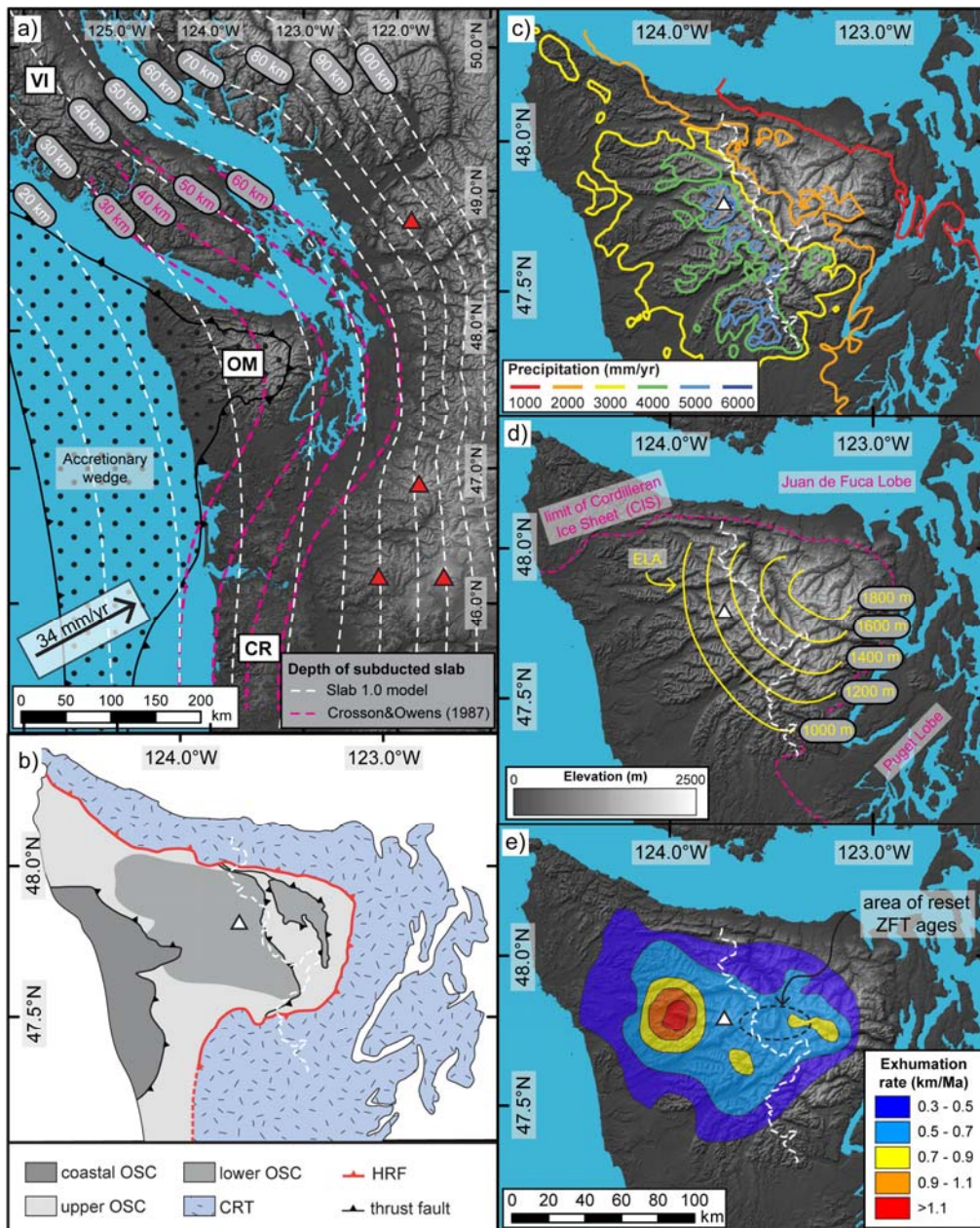


Figure DR1: (a) Overview of the Cascadia subduction zone at the latitude of the Olympic Mountains, convergence velocity of 34 mm/yr from Dourovine and Tarduno (2008), dashed lines show the location of the top of the subducted slab at depth, Slab1.0 is based on McCrory et al. (2012), note that McCrory et al. (2012) refer to the top of the slab as the top of the oceanic igneous crust, whereas Crosson and Owens (1987) refer to it as the oceanic Moho, red triangles denote active volcanoes, VI = Vancouver Island, OM = Olympic Mountains, CR = Coast Range. (b) Structure of the Olympics, based on Tabor and Cady (1978) and Brandon et al. (1998), OSC = Olympic Structural Complex, CRT = Coast Range Terrain, HRF = Hurricane Ridge Fault. (c) Precipitation pattern from the PRISM data set (www.prism.oregonstate.edu). (d) Extent of the Cordilleran Ice Sheet and location of the equilibrium line altitude (ELA) on the peninsula, after Porter (1964). (e) Exhumation rate pattern as derived from the inversion of AFT data (Brandon et al., 1998), area of reset ZFT ages is based on Brandon and Vance (1992). In all panels, the white triangle and the thin white dashed line denote the location of Mt. Olympus or the range divide, respectively.

The strong orographic rainshadow effect in the Olympics is shown in Figure DR1c. Areas on the western side of the mountain range receive 5000 – 6000 mm/yr of precipitation, whereas the eastern part of the range is much drier and partly receives < 1000 mm/yr of precipitation.

The Olympics were strongly impacted by glacial processes. The Cordilleran Ice Sheet (CIS) advanced from the Coast Mountains in British Columbia down to the latitude of the Olympic Mountains several times during the Pleistocene (Easterbrook, 1986), and the Juan de Fuca and Puget lobe surrounded the range in the north and east/south east, respectively (Porter, 1964, see Figure DR1d). Due to the presence of the CIS it is difficult to reconcile the extent of alpine glaciation on the northern and eastern side of the peninsula, because alpine ice streams merged with the CIS or deposits from alpine glaciers were destroyed by later advances of the CIS. Contrary to that, the western side of the peninsula offers well preserved glacial deposits (Figure 1a in the main text), suggesting that piedmont-style alpine glaciers initiating in the headwaters of Hoh, Quinault or Queets valleys almost advanced to the Pacific ocean (Thackray, 2001). Similar to the distribution of rainfall, the equilibrium line altitude (ELA) shows a strong spatial gradient (Figure DR1d) and increases from 1000 m on the western side to 1800 m on the eastern side (Porter, 1964).

It is difficult to exactly determine, when Pleistocene glaciation initiated in the Olympic Mountains. The oldest, preserved remnants from the CIS in the area were found south of Seattle (Easterbrook, 1986) and belong to the Orting drift. They are believed to be ~2 Ma old, however, due to the magnetic polarization of the deposits, they could be deposited anytime between 0.78 and 2.48 Ma. Remnants of older alpine, glaciations are scarce within the Olympic Mountains, but deeply weathered glacial deposits on the western peninsula are believed to be of the same age as the Orting drift (Easterbrook, 1986). A marine drill core (OPD leg 168, at 48°N, 200 km offshore from Vancouver Island) shows a transition from deep sea sedimentation to turbidity current derived sedimentation at 1.7 Ma (Underwood et al., 2005). This could indicate increased turbidity current activity due to higher sediment supply, caused by increased glacial erosion. Generally, the offshore sedimentation increased significantly during the Quaternary and even led to a change in deformation of the accretionary wedge (e.g. Adam et al., 2004)

The exhumation rate pattern suggested by Brandon et al. (1998) based on inversion of their AFT data suggests fastest exhumation rates (>1.0 km/Ma) at the confluence of the north and south fork Hoh rivers (see Figure DR1e). Lower rates (~0.7 km/Ma) prevail in the center of the range. However, the only area of reset zircon fission track ages (13 – 14 Ma) is to the east of Mt. Olympus (Brandon and Vance, 1992).

DR2. THERMOCHRONOMETRIC DATING

DR2.1 Details for sampling

Where possible, we preferred sandstone to siltstone/slate while sampling. The collected sandstones vary in color, grain size and mineral composition (especially in feldspar, mica and lithics content). Location of the samples within the Olympics is shown in Figure DR2, coordinates and elevation together with the final ages for each sample can be found in table DR1. A map of ages is shown in Figure DR3.

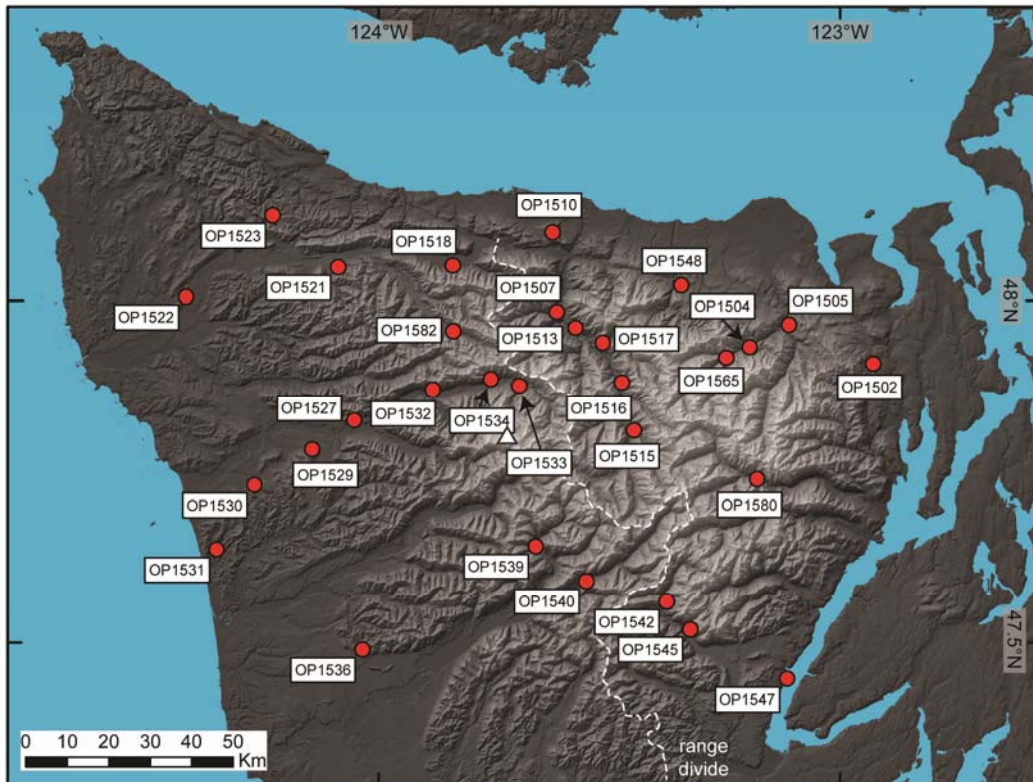


Figure DR2: Samples collected for this study and their location on the Olympic Peninsula. White triangle denotes location of Mt. Olympus.

DR2.2 Analytical procedure for thermochronometric dating

Common mineral separation techniques involving density and magnetic separation are applied to get apatite and zircon separates. Mineral grains are hand-picked under air in the thermochronology labs at the University of Tübingen using a Leica microscope. Euhedral, inclusion-free grains are selected and packed in Nb-tubes. Especially for apatite this often proves to be difficult due to the detrital nature of the rocks. Hence, sometimes smaller but well-shaped grains (<70 μm) are packed. Apatite and zircon grains are analyzed in the thermochronology labs at the University of Tübingen and the further measurement procedure follows Stübner et al. (2016) and is described there. Parameters for Ft-correcting the AHe and ZHe ages are taken from Farley (2002) and Hourigan et al. (2005), respectively. The approach used for solving the (U- Th)/He age equation follows the method of Meesters and Dunai (2005). For each sample, 3 – 5 grains are dated for AHe and three grains for ZHe. Data for the single grain analyses for apatite and zircon are reported in excel-tables DR2 and DR3, respectively.

Table DR1: Overview of the samples, providing coordinates, AHe ages, ZHe ages and depositional age of the samples (depositional age after Brandon et al. (1998); Tabor and Cady (1978)). nd = not determined.

Sample	North (°)	East (°)	Elevation (m)	AHe age (Ma)	AHe 1SD (Ma)	ZHe age (Ma)	ZHe 1SD (Ma)	probable depositional age
OP1502	47.90796	-122.92804	325	unreset	-	unreset	-	late Eocene 40 - 34 Ma
OP1504	47.93233	-123.19509	675	4.6	1.4	unreset	-	lower - middle Eocene 55 -43 Ma
OP1505	47.96524	-123.11056	314	6.2	1.6	unreset	-	lower - middle Eocene 55 -43 Ma
OP1507	47.98305	-123.61359	453	3.3	0.2	14.3	1.9	Eocene 34 - 55 Ma
OP1510	48.09852	-123.62231	273	8.3	1.2	unreset	-	upper Eocene - Oligocene 37 - 24 Ma
OP1513	47.96015	-123.57273	402	1.5	0.3	10.2	1.0	Eocene 34 - 55 Ma
OP1515	47.81031	-123.44630	537	2.8	0.7	5.9	0.5	early Eocene 34 - 55 Ma
OP1516	47.88040	-123.47196	426	nd	-	7.7	1.1	late Oligocene - early Miocene 26 - 20 Ma
OP1517	47.93891	-123.51376	423	3.7	0.9	9.0	0.6	late Oligocene - early Miocene 26 - 20 Ma
OP1518	48.05061	-123.83886	223	8.6	1.5	nd	-	lower - middle Eocene 55 - 43 Ma
OP1521	48.04832	-124.08702	390	2.0	0.4	unreset	-	Eocene 55 - 34 Ma
OP1522	48.00530	-124.41620	367	9.1	0.9	unreset	-	late Oligocene - early Miocene 26 - 20 Ma
OP1523	48.12315	-124.22835	363	6.8	1.1	nd	-	upper Eocene - Oligocene 37 - 24 Ma
OP1527	47.82500	-124.05184	280	2.8	1.0	unreset	-	late Oligocene - early Miocene 26 - 20 Ma
OP1529	47.78265	-124.14257	343	6.2	1.1	unreset	-	late Oligocene - early Miocene 26 - 20 Ma
OP1530	47.73081	-124.26813	221	10.4	1.3	unreset	-	early - middle Miocene 20 - 14 Ma
OP1531	47.63659	-124.34966	50	7.5	0.5	unreset	-	early - middle Miocene 20 - 14 Ma
OP1532	47.87025	-123.88135	323	1.8	0.6	6.6	2.5	late Oligocene - early Miocene 26 - 20 Ma
OP1533	47.87572	-123.69427	430	2.5	0.4	4.8	0.6	late Oligocene - early Miocene 26 - 20 Ma
OP1534	47.88536	-123.75552	475	2.1	0.2	6.5	1.2	late Oligocene - early Miocene 26 - 20 Ma
OP1536	47.48917	-124.03370	390	7.5	0.8	unreset	-	
OP1539	47.64151	-123.65870	446	2.1	0.6	6.8	0.4	late Oligocene - early Miocene 26 - 20 Ma
OP1540	47.59012	-123.54913	367	1.5	0.6	6.2	0.6	late Oligocene - early Miocene 26 - 20 Ma
OP1542	47.56001	-123.37533	450	1.9	0.7	8.6	0.9	early Eocene (?)
OP1545	47.51918	-123.32442	390	15.0	2.9	nd	-	lower - middle Eocene 55 - 43 Ma
OP1547	47.44632	-123.11424	11	unreset	-	unreset	-	Oligocene - lower Miocene 34 - 21 Ma
OP1548	48.02186	-123.34295	407	14.8	2.1	unreset	-	Oligocene (upper Eocene) 34 -24 Ma
OP1565	47.91644	-123.24616	720	4.7	1.9	13.8	1.7	Eocene 34 - 55 Ma
OP1580	47.73972	-123.17929	509	5.0	1.2	10.0	1.5	Eocene 34 - 55 Ma
OP1582	47.95595	-123.83732	578	1.7	0.5	7.1	0.5	late Oligocene - early Miocene 26 - 20 Ma

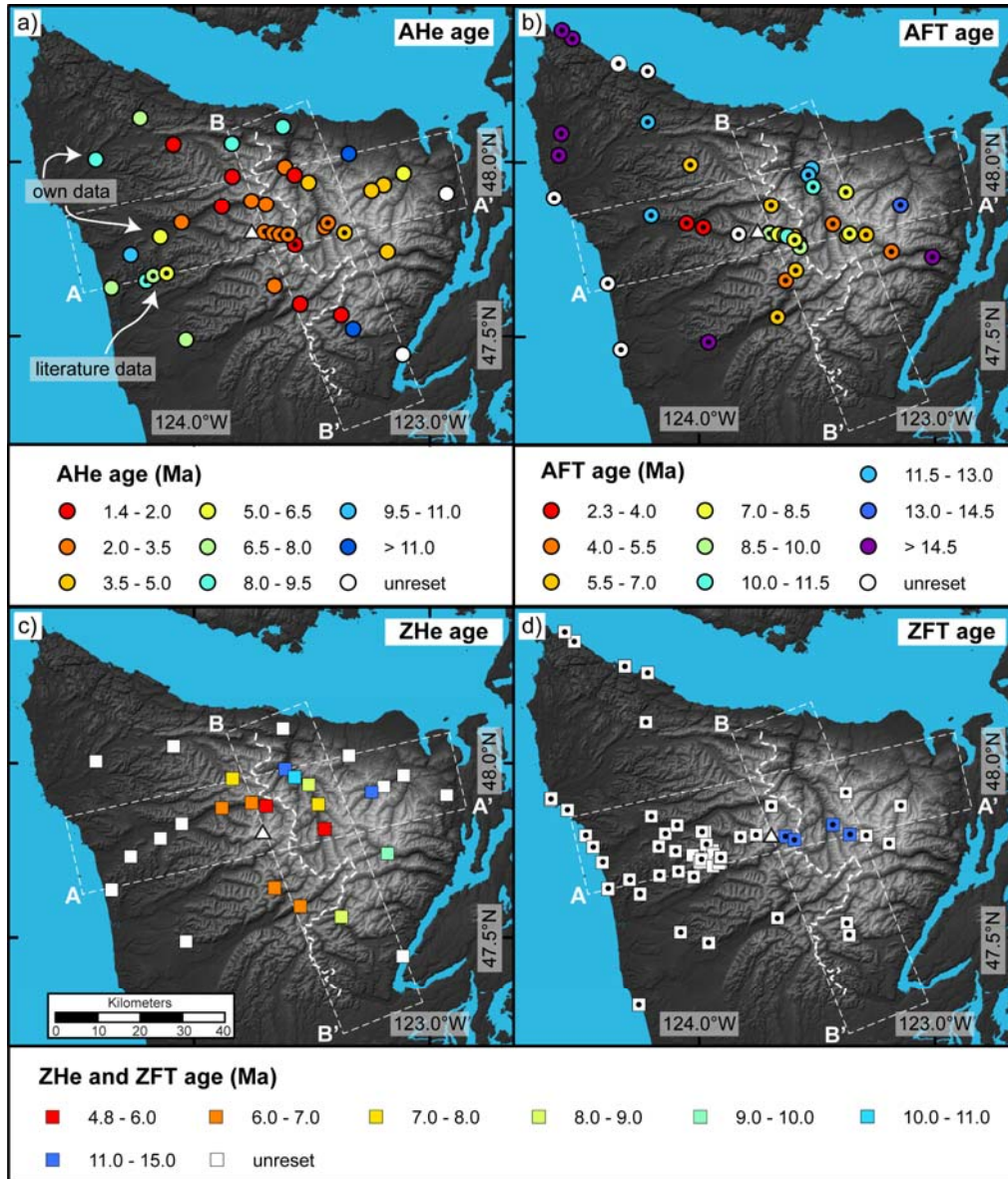


Figure DR3: Compiled map of the thermochronometry data available for the Olympic Mountains. AHe and ZHe are from this work, literature AHe data are taken from Batt et al. (2001), AFT is from Brandon et al. (1998) and ZFT from Brandon and Vance (1992) and Stewart and Brandon (2004). Note that our data are collected at an equal elevation of 400 m, whereas the literature data are not. The white dashed line denotes the range divide and the white triangle Mt. Olympus, respectively. White boxes outline the swaths parallel and perpendicular to the range divide.

To calculate the sample ages from the single grain ages, we use the Helioplot software package (Vermeesch, 2010). However, we do not use the recommended central age as sample age, but instead use the arithmetic mean age. In our case, the errors for the central age are very large for some samples, which is probably caused by the very different composition of the mineral grains in these detrital samples. This effect is also enhanced by the small number of mineral grains

that we only date per sample ($n=3 - 5$). As uncertainty Helioplot states the standard error (1SE), which we then use to calculate the standard deviation (1SD) that is reported in our data table.

In general, the geologic uncertainty that is inherent in (U-Th-Sm)/He dating is larger than the analytic uncertainty, which results in very different and overdispersed single grain ages within one sample. This geologic uncertainty is caused by overseen inclusions in the mineral grains, radiation damage or factors that affect the Ft-correction (e.g. grain shape, strong U/Th-zonation). As further complication in our case, it is possible, that a sample is not fully reset and the mineral grains still record a signal from the source region of the sandstones, as is the case with published AFT and ZFT data for the study area (Brandon and Vance, 1992; Brandon et al., 1998). Likewise, this creates problems using common methods for outlier detection. Our approach for determining, whether the range in single grain ages is caused by the geologic uncertainty or by the unreset/partially reset nature of the sample is as follows.

First, samples that only contain single grain ages older than the onset of exhumation in the Olympics (18 Ma, Brandon et al., 1998) or where the single grain ages are similar to/older than the depositional age of the sample (see table DR1) are considered unreset. Samples, which pass this first test, are checked, whether they still show a large spread in single grain ages and if grains do not overlap within 2SD of their respective analytic uncertainty, the particularly old or young grains are considered as possible outliers. However, due to our small number of grains dated per sample (3 – 5), we can not discern between fully reset, partially reset or multiply reset samples (e.g. Brandon et al., 1998).

The detrital nature of our sandstone samples, and linked to this the poor sample quality and different chemical composition of single grains likely also impacts the reproducibility of measured ages. For the analyzed apatites the mean standard deviation is ~21% (1 sigma, 27 samples, 92 dated grains, outlier grains and grains from unreset samples excluded). For the dated zircon grains the mean standard deviation is ~13 % (1 sigma, 14 samples, 34 dated grains, outlier grains and grains from unreset samples excluded). The poor reproducibility for our AHe ages is probably also linked to the very low He content of many grains, which is caused by the young age of many samples and the partly volcanic origin of apatite grains (these contain low amounts of U and Th and hence He). High uncertainties of up to 30% for apatite single grains from young samples supports this hypothesis. Comparison with the reproducibility of standards measured in the thermochronology labs of the University of Tübingen (for Durango apatite 6%, $n=24$; for Fish Canyon Tuff zircons 6%, $n=21$) indicates that indeed our observed reproducibility is likely caused by the nature of our samples and not by analytical issues.

DR3. DETAILS FOR THERMO-KINEMATIC MODELING

DR3.1 General setup for the models

For our numerical modeling purpose we use the 3D thermo-kinematic model Pecube-D (e.g. Whipp et al., 2009; McQuarrie and Ehlers, 2015), which allows to calculate thermochronometric cooling ages from time-temperature paths and compare these modeled ages with our data. The model domain encompasses almost the entire Olympic Peninsula (120 km x 140 km, see Figure DR 4) and the depth of the model is 20 km, which corresponds to the minimum thickness of the accretionary wedge

beneath the Olympic Mountains (e.g. Davis and Hyndman, 1989). Further model parameters are summarized in table DR4. For elevation, we use the present day topography, which is derived from a 10 m digital elevation model and downscaled, so that the final resolution of the model is 500 m. In order to better recognize modeled, unreset ages, we initiate our models at 50 Ma. Following Brandon et al. (1998), we start exhumation at 18 Ma and reach steady state at 14 Ma, which implies steady, present-day topography for the remaining model duration. This seems counterintuitive, because glaciation significantly impacted the topography of the mountain range. However, considering changes in topography within the model requires knowledge of the pre-glaciation topography, which we are not able to provide. So in order to reduce the model complexity and to not use unconstrained parameters, we keep the topography constant.

Table DR 4: List of parameters used for the Pecube modeling.

Parameter	Value	Source
thermal conductivity	1.83 W m ⁻¹ K ⁻¹	average value for six drill cores in sediment material in the shelf offshore from Vancouver Island (Lewis et al., 1988)
Specific heat capacity	1200 J kg ⁻¹ K ⁻¹	
crustal density	2700 kg m ⁻³	
mantle density	3200 kg m ⁻³	
temperature at the base of the model	400 °C	extrapolation to greater depths from temperature estimates based on heat flow measurements on the shelf (Hyndman et al., 1990; Hyndman and Wang, 1993; Booth-Rea et al., 2008)
temperature at sea level	8 °C	
atmospheric lapse rate	6.69 °C km ⁻¹	
crustal heat production	0.77 μW m ⁻³	average value from drill cores on the shelf offshore from Vancouver Island (Lewis and Bentkowski, 1988)

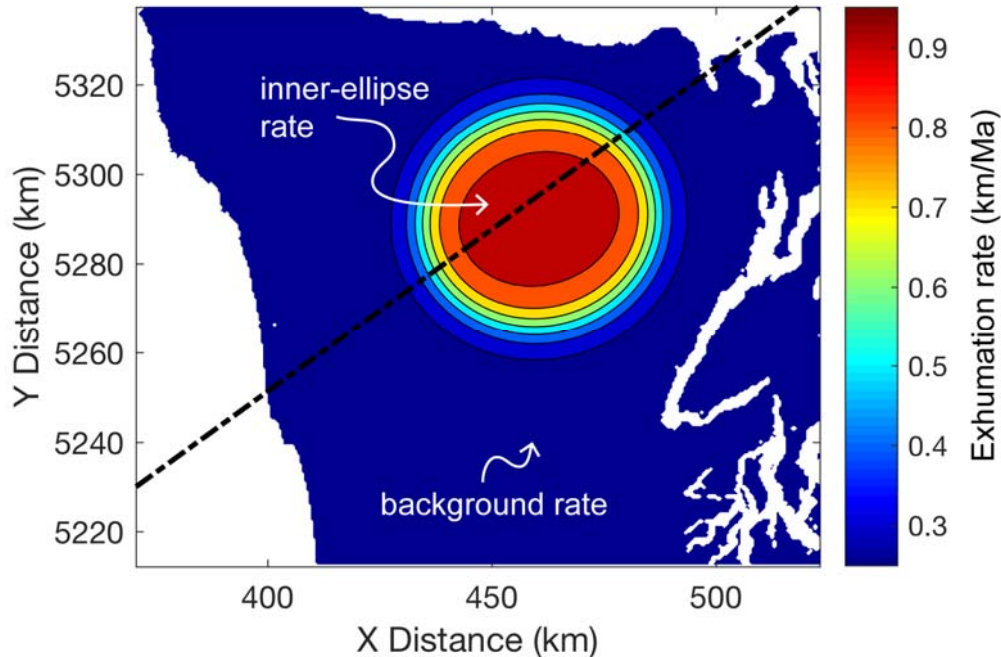


Figure DR4: Elliptic exhumation rate pattern used for our model runs. Rates are defined outside of the ellipse (background rates), where they are lowest and in the inner ellipse, where they are highest. The pattern and values shown (0.25 to 0.9 mm/yr) are for our preferred constant rate ellipse. Rates for the horizontal model runs (section DR3.3) were extracted along the black, dashed line. Offshore above the ocean exhumation rates are set to zero.

DR3.2 Vertical-velocity-only models

DR3.2.1 Constant, long-term exhumation rates

Spatial variations in exhumation rates in the Olympic Mountains have already previously been reported for the Olympic Mountains (Brandon et al., 1998; Batt et al., 2001). Hence, we explored which pattern best explains the observed ages from our study (AHe and ZHe) and the literature data (AHe, AFT and ZFT). We run our models only considering vertical velocities and use an elliptic shaped exhumation pattern (for discussion of horizontal velocities see section DR3.3). Maximum exhumation rates are defined in the inner ellipse and minimum rates (“background rates”) outside of the ellipse (see Figure DR4). Pecube interpolates smoothly between these two values, to get the further values. Furthermore, in order to reconstruct transient changes in exhumation in the Olympic Mountains with onset of Pleistocene glaciation, we use a two-step approach.

First, in order to estimate the best long-term exhumation history, we use constant rates throughout the entire model duration and try to find the best-fit ellipse in terms of location, size and rates. The location and size of the ellipse are assessed by the general pattern of reset/unreset ages. The most appropriate rates for the ellipse are found by using a reduced χ^2 -test. We perform runs with five different inner ellipse rates (0.8, 0.9, 1.0, 1.2, 1.4 km/Ma) and six different background rates (0.1, 0.2, 0.25, 0.3, 0.4, 0.5 km/Ma). At first we look at the distribution of single χ^2 -values for each sample and each model run in order to get an overview of how well the

models reproduce the ages. The χ^2 -value gives information about the misfit between predicted (τ_m) and observed ages (τ_o with uncertainty σ_o):

$$\chi^2 = \left(\frac{\tau_o - \tau_m}{\sigma_o} \right)^2$$

In order to also assign an uncertainty to unreset samples and include them in the χ^2 -test, we use an “arbitrary” uncertainty of 10%. Following Adams et al. (2015) we also apply this approach to reset samples and either use the actual uncertainty or use the 10%, whichever is greater. Furthermore, because Pecube can not discern between fully and partially reset samples, we exclude all AFT and ZFT samples from the data set that do not show concordant ages. Figure DR5 displays the range of observed χ^2 -values for each thermochronometric system. Generally the misfit for AFT and ZFT is smaller ($\chi^2 < 100$) compared to AHe or ZHe, where the χ^2 -values can be as high as 10^4 and can display a range of several magnitudes for some samples. Samples that have these very high χ^2 -values are likely candidates that can distort and bias a reduced χ^2 -analysis. Hence, we excluded several samples from the further analysis. This includes samples OP1521 and OP1582 for AHe (sample number 14 and 33 in Figure DR5), and samples OP1532, OP1542 and OP1582 for ZHe (sample number 16, 22 and 27 in Figure DR5). One reason why these samples show particularly high χ^2 -values could be that the true shape of the exhumation rate pattern deviates from the imposed perfectly ellipse-shaped pattern.

So we use a total of 31 AHe, 14 AFT, 24 ZHe and 45 ZFT ages for our reduced χ^2 -analysis. For the respective thermochronometer system, the reduced χ^2 -value is defined as the sum of the single χ^2 -values from each sample divided by the number of samples (n):

$$\chi_{reduced}^2 = \frac{1}{n - 2} \sum \left(\frac{\tau_o - \tau_m}{\sigma_o} \right)^2$$

The resulting reduced χ^2 -values for assessing the best-fit ellipse are displayed in Figure DR6 and give information about the goodness of fit for the respective combination of outer/inner ellipse rates. Comparing the best-fit suggestions (outlined by the red box in the subpanels in Figure DR6) for the four thermochronometer systems shows that very different combinations of outer/inner ellipse rates are suggested for each thermochronometer system (e.g. 0.25/1.2 for ZHe vs. 0.25/0.8 for AFT vs. 0.5/1.2 for AHe). This indicates that there is likely no single constant exhumation rate history fitting all thermochronometer systems equally well. Thus, simply adding the reduced χ^2 -values from each system to a total χ^2 -value could lead to a biased combination of outer/inner rates (e.g. this approach would favor 0.25/1.2 km/Ma, giving an almost perfect fit for ZHe, but significantly misfitting AHe and to a minor amount AFT and ZFT). Furthermore, high rates in the inner ellipse (>1.0 km/Ma) result in ZFT ages that are much too young, compared to their unreset age or to the four partly reset ZFT ages (modeled ages of 5 – 10 Ma vs. 13 – 14 Ma for the reset samples). Choosing a high value in the inner ellipse results already in a very good fit for ZHe with constant exhumation rates (e.g. a reduced χ^2 -value of 1 – 2). However, a later increase in rates (which is suggested by the bad fit of constant rate models for AHe) would lead to very young ZHe ages and again decrease the reduced χ^2 -values for ZHe.

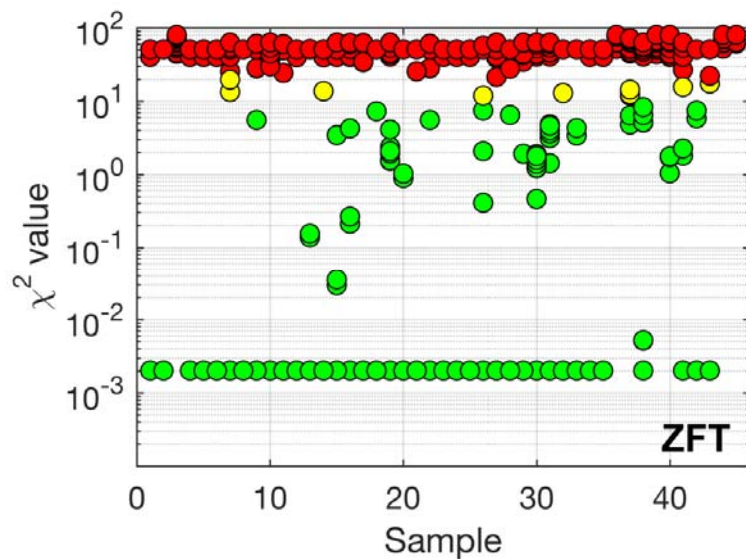
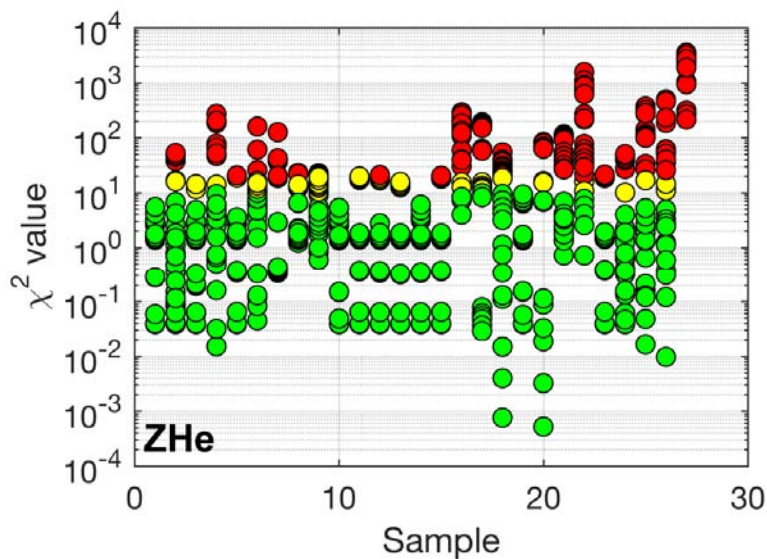
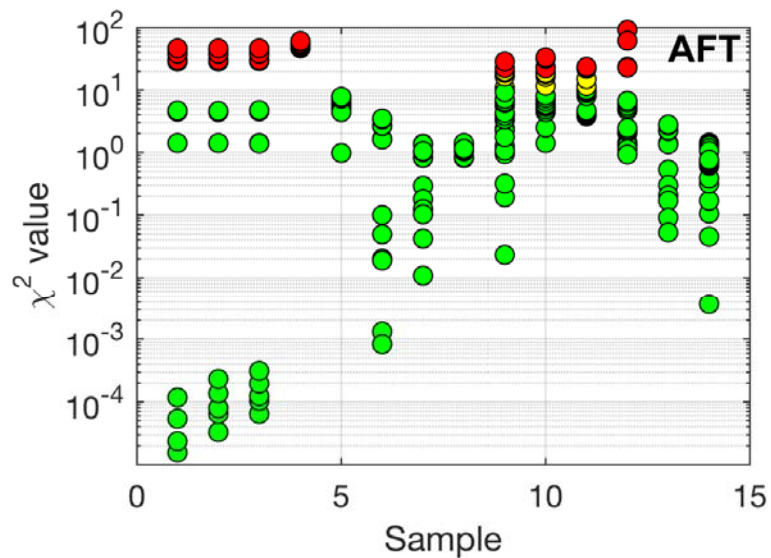
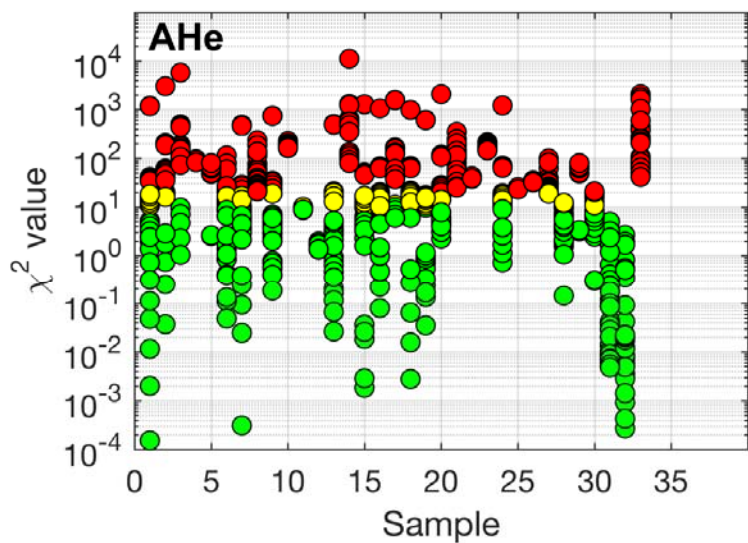


Figure DR5: Range of χ^2 -values for AHe, AFT, ZHe and ZFT from investigating the best-fit ellipse in terms of inner ellipse rate and background rate. Each point corresponds to the outcome from one single model run, so in total 30 points are shown for each sample (5 inner ellipse rates and 6 background rates give 30 possible combinations). The color coding corresponds to the goodness of fit: green symbols $\chi^2 < 10$, yellow χ^2 between 10 and 20, red $\chi^2 > 20$. In general the AHe and ZHe ages are more difficult to fit and their χ^2 -values can have a range of several orders of magnitude. Some AHe and ZHe samples have high χ^2 -values ($\chi^2 > 1000$) and are particularly difficult to fit, hence we excluded them from the further reduced χ^2 -analysis. This includes samples 33 and 14 for AHe, and 27, 22 and 16 for ZHe. Note that the y-axes are logarithmic.

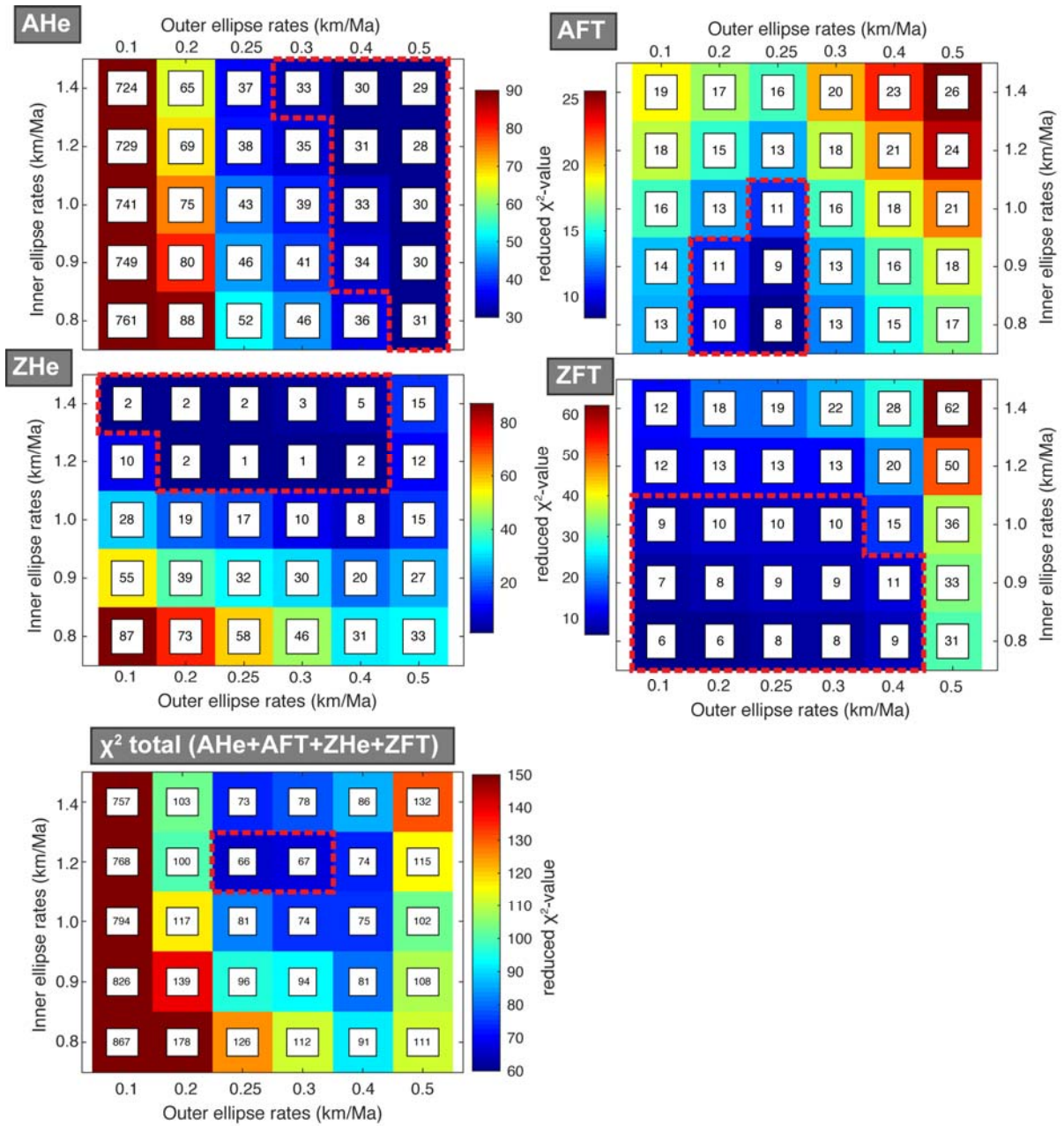


Figure DR6: Results from finding the best-fit constant rates for the ellipse, showing the reduced χ^2 -values for AHe, AFT, ZHe, ZFT and the sum of all systems from our reduced χ^2 -test runs. We performed model runs with five different erosion rates in the inner ellipse and six different background/outer ellipse erosion rates. Best fit solutions for each system are indicated by red boxes, note that the best-fit combinations of inner/outer ellipse rates differ significantly for the different thermochronometer systems. The colorbar is different for each subpanel.

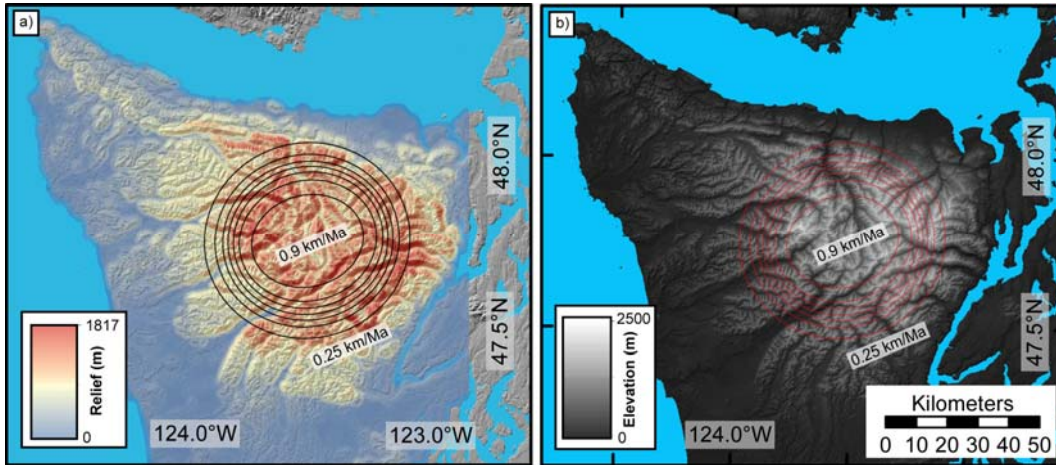


Figure DR7: Maps of a) relief (calculated for a moving circle of 3 km diameter) and b) elevation compared to our best-fit ellipse pattern. Both areas of high relief and elevation are contained within our ellipse pattern.

To conclude, due to the afore mentioned points we argue for an inner ellipse rate that is not too high and picked rates of 0.25/0.9 km/Ma for our preferred constant-rate ellipse. This combination is strongly favored by AFT and ZFT (each have reduced χ^2 -values of 9), and if rates are increased within the transient model runs for the 0.25/0.9 km/Ma ellipse, the total χ^2 -values are also lower (~ 50 for best-fit transient models, see below) compared to the 0.25/1.2 km/Ma ellipse suggested by the total χ^2 -values (66). Different from Brandon et al., (1998) we do not locate the center of our ellipse on the western side (see Fig. DR1e), but in the central high topography part of the mountain range. Here, highest rock uplift rates are suggested to correlate with mean elevation and relief (Adams and Ehlers, 2017). Our proposed ellipse pattern matches both relief and mean elevation, where areas of highest relief and elevation are contained within the ellipse (Fig. DR7)

DR3.2.2 Transient model runs

In a second step, we use these best-estimate long-term exhumation rates (0.25 - 0.9 km/Ma) in order to explore transient model runs, where the exhumation rate is increased. This is centered around the question, whether Pleistocene glaciation, which undoubtedly affected the topography in the Olympics (e.g. Montgomery and Greenberg, 2000; Montgomery, 2002; Adams and Ehlers, 2017), also had an influence on the exhumation of the mountain range.

Considering transient model runs adds more parameters to the model space that could be variable and that need to be explored. Hence, we try to find the best timing of increase in rates as well as increase amount by again using a reduced χ^2 -test. For this we consider six times of increase (1, 2, 3, 5, 7 and 10 Ma) and seven increase amounts (10, 30, 50, 70, 100, 150 and 200%, all measured relative to the best-fit ellipse rate of 0.25/0.9 km/Ma), resulting in 42 possible increase histories. Values from the reduced χ^2 -test for each thermochronometer system and the total reduced χ^2 -value (sum of all systems) for each increase history are shown in Figure DR8, where the best-fit solutions with the lowest χ^2 -values are outlined by red boxes. Transient model runs with increasing exhumation rates lead to a much better fit of

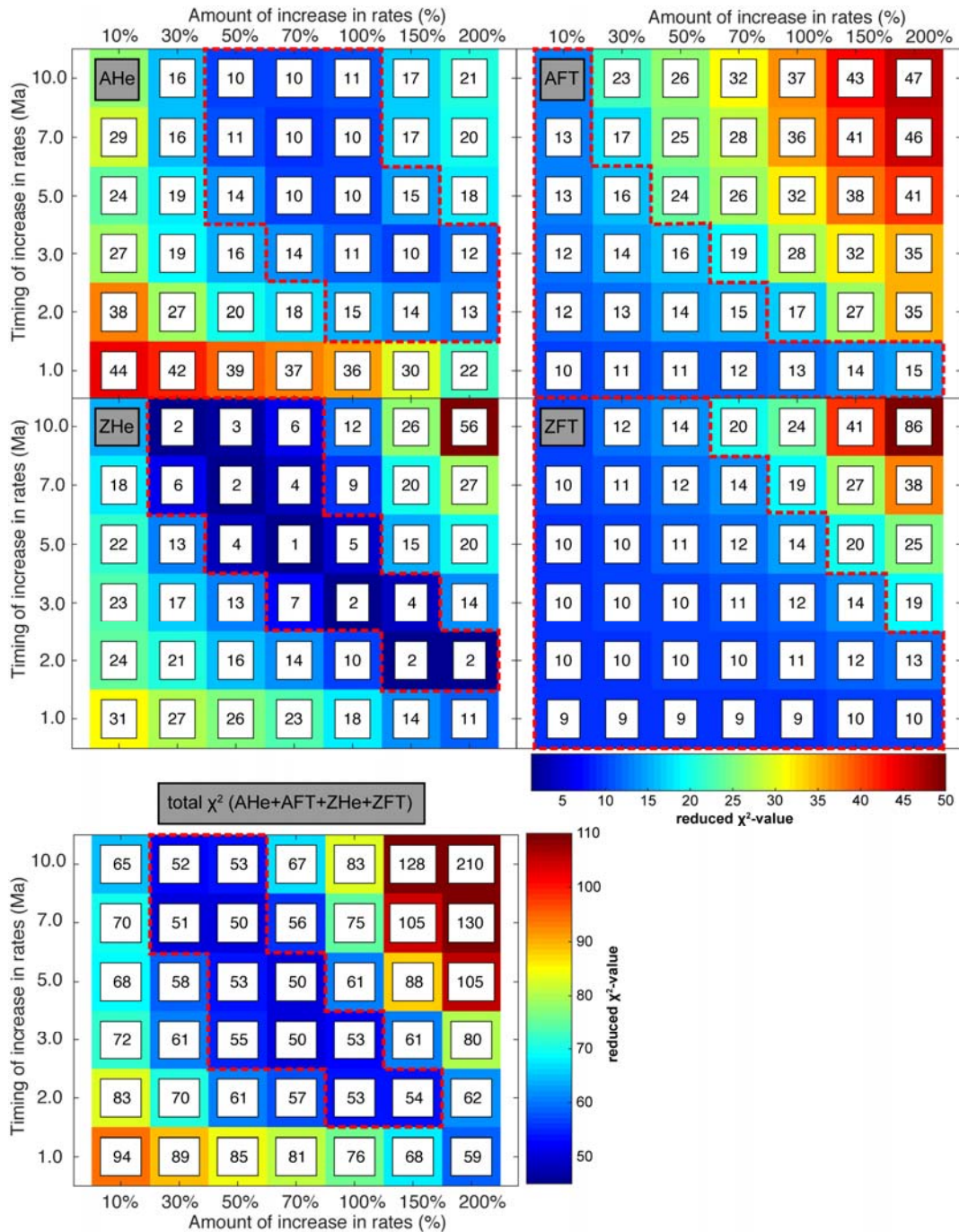


Figure DR8: Results from finding the best-fit transient model run, where the timing of an increase in exhumation rates (6 different times) and the magnitude of increase (7 different amounts) are varied, giving a total of 42 possible combinations. Shown are the reduced χ^2 -values for AHe, AFT, ZHe, ZFT and the sum of the four systems. Best-fit solutions are outlined by red boxes in each subpanel. This indicates, that several increase histories equally well fit the data, e.g. an earlier increase requires a smaller amount, compared to a later increase with higher increase in exhumation rate. The amount of increase is measured relative to the best fit ellipse, which has rates of 0.25/0.9 km/Ma.

AHe ages (reduced χ^2 -values of 10 – 15 compared to 29 – 34 for constant models, see Figures DR6 and DR8). Furthermore, ZHe now also shows a much better fit (reduced χ^2 -values of 1 – 7, compared to 32 for the constant 0.25/0.9 model run). Reduced χ^2 -values for AFT and ZFT do slightly increase for the transient model runs, probably because the modeled ages for unreset samples become even younger with increased rates. In summary, the total reduced χ^2 -value for the transient models (50 – 55) is lower than for the best-fit constant rate model (66) and suggests that an increase in exhumation rate is required to explain the observed ages. However, this also shows that there is a non-unique solution and that several exhumation histories give an equally good fit (Figure DR8): at 2 Ma 100 – 150% increase, at 3 Ma 50 – 100% increase, at 5 Ma 50 – 70% increase and at 7 or 10 Ma 30 – 50% increase. So the earlier the timing of increase, the smaller is the required amount of increase in rates. A summary of our preferred simulations can be found in table DR 5.

Although the model suggests that an increase in rates could happen at different times, there also needs to be an increase mechanism preserved in the geological record at this particular time step, to make this timing of increase geologically feasible. To our knowledge, there is no mechanism between 5 – 10 Ma, that could result in an increase in exhumation rates, e.g. the subduction zone geometry is thought to be in its present day geometry since the latest Eocene (Brandon and Vance, 1992), exhumation of the Olympic Mountains started already at 18 Ma (Brandon et al., 1998), and no significant change in climate has been proposed for this period. On the other hand, Pleistocene glaciation shaped the Olympic Mountains, both by alpine glaciers (see e.g. Figure 1 in the main paper) and the Cordilleran Ice Sheet (Figure DR1d). So Pleistocene glaciation is a mechanism readily at hand and has been invoked as a reason for changes in exhumation on a world-wide scale (e.g. Herman et al., 2013), but also local studies in other orogens suggest a strong impact of Pleistocene glaciation, e.g. in the Coast Mountains of British Columbia (Ehlers et al., 2006), St. Elias Range of Alaska (e.g. Berger et al., 2008) or the European Alps (e.g. Glotzbach et al., 2013).

The exact onset of alpine glaciation in the Olympic Mountains is difficult to determine (see discussion in chapter DR1), hence we also collected information about Pleistocene glaciation in nearby areas in order to present a possible time frame for glaciation. Onset of alpine glaciation in the Olympics could be as old as 2 Ma (Easterbrook, 1986) and is close to the proposed onset of northern hemisphere glaciation at 2.7 Ma (Haug et al., 2005). However, glaciation commenced as early as 7 – 8 Ma in the BC Coast Mountains (Clague, 1989; Ehlers et al., 2006), only 400 km north of the Olympics. Given these time constraints, we believe that 2 to 3 Ma are plausible timings for increasing exhumation rates and picked these times and the suggested increase amounts (at 2 Ma 100 – 150% increase, at 3 Ma 50 – 100% increase) as our preferred transient model solutions. Our proposed range of increasing rates by 50 – 150% is also in accordance with results from the BC Coast Mountains (Ehlers et al., 2006) and would correspond to an ellipse with outer/inner rates of 0.38/1.4 – 0.63/2.3 km/Ma. Furthermore, a peak in glacial erosion at 1.8 ± 0.2 Ma in the BC Coast Mountains (Shuster et al., 2005) suggests, that the effect of glacial erosion on exhumation can be temporally variable, and hence offering a range of increase times and amounts is geologically meaningful.

Table DR 5: Summary of our preferred transient thermo-kinematic simulations from Figure DR8.

Amount of increase relative to constant rate	Outer/Inner ellipse rates (km/Ma)	Onset times for an increase in rates				
		2 Ma	3 Ma	5 Ma	7 Ma	10 Ma
Initial constant rate	0.25/0.9					
10%	0.28/1.0	-	-	-	-	-
30%	0.33/1.2	-	-	-	X	X
50%	0.38/1.4	-	X*	X*	X	X
70%	0.43/1.5	-	X*	X*	-	-
100%	0.5/0/1.8	X*	X*	-	-	-
150%	0.63/2.3	X*	-	-	-	-

Notes: X = Respective increase at respective time yields best-fit simulation.

- = Respective increase at respective time did not yield a best-fit simulation

* = Results from simulations are displayed in Figure 2.

In order to finally compare sample ages with model ages (Figures 2b,c,e,f in the main paper), we use the following approach. Model ages from the preferred transient model runs are extracted along the swaths A/A' and B/B', both with a width of 30 km. For better comparison with our equal elevation data (collected at ~400 m), these model ages are filtered for elevations between 200 and 500 m in a next step and the mean ages are calculated for each increment of the swath from the filtered ages. Finally, the colored envelopes in Figure 2b,c,e,f represent the range of ages derived from the five preferred transient model runs and are compared to the constant model run with the 0.25/0.9 km/Ma ellipse (black, solid lines in Figure 2b,c,e,f). For reference, the results for an earlier increase in rates (50 and 70% at 5 Ma) are also displayed, and given the uncertainty with onset of glaciation in the Olympics, the effect of glaciation commencing at this time would still produce ages observed in the Olympics.

As elaborated in chapter DR1, both precipitation and the location of the equilibrium line altitude (ELA) show strong west to east gradients within the Olympics (Figures DR1c,d) and the ELA is lowest on the west side. Because the ELA corresponds to the area of most effective glacial erosion (e.g. Montgomery, 2002), the effect of glacial erosion on the exhumation rate is also expected to vary spatially in the Olympics. This is already partly reflected by the range of viable increase amounts of our models (50 – 150%). But particularly samples on the western side of the range (OP1527, OP1529, OP1532) still have AHe ages that are younger than ages predicted by our preferred transient model runs. So locally an increase by 150 – 200% or even more could explain the observed, young AHe ages (see range of predicted ages for this amount of increase in Figure 2b).

We do not include the literature data in our swath profiles of Figure 2, because direct comparison between our own data and the published literature data is

hampered, due to the different (non-constant elevation) sampling approach. Our own samples were collected at an equal elevation of ~400 m allowing for direct comparison between the samples (where the effect of topography on thermochronometric ages does not have to be considered). On the other hand, the literature samples were collected at elevations between sea level and 2400 m. Nevertheless, we use the fully reset AFT ages in our χ^2 -approach in order to assess the goodness of fit for our transient model runs (Figure DR8). Furthermore we provide a comparison of literature AFT and ZFT ages to modeled ages along the swaths in Figure DR9, where we considered literature samples from elevations between 0 and 600 m asl (to make these swaths comparable to Figure 2). However, not many samples are available within this elevation range. The observed fit of sample to modeled ages is not as good as for our own AHe and ZHe data, particularly AFT ages seem to be too old. Several reasons could account for that. All of our and literature samples collected in the Olympic Mountains are sandstones and are hence detrital in nature, if they have not been subducted deep enough and heated to reset them. For their AFT ages this leads Brandon et al. (1998) to discern between fully reset (single age peak, younger than depositional age of sample), partially reset (several peaks, one age peak younger than depositional age), multiply reset (several age peaks, all younger than depositional age) and detrital samples (all peaks older than depositional age). The distribution of the different sample types is not correlated with their spatial occurrence, because fully, partially and multiply reset samples can all be found in the interior of the mountain range. This clearly indicates that the resetting process is variable from sample to sample. Due to the different kinetics of the AHe, AFT and ZHe systems differences in the resetting behavior for these systems seem to be plausible. This could partly account for the better fit of AHe and ZHe ages to our models, compared to AFT, especially since modeled ages within Pecube are treated as fully reset ages. Furthermore, the quality of some of the sandstone samples from the Olympics can be poor and can cause analytical difficulties. E.g. for some of their fully reset samples Brandon et al. (1998) were able to report only 9 – 13 grains, although usually 20 grains should be dated for AFT dating purposes. Finally, one further aspect that could result in a good fit of AHe and ZHe but a bad fit of AFT ages is another variation in exhumation rates besides our proposed increase at 2 Ma like a decrease in rates after samples cooled through the closure temperature of ZHe and subsequent stronger increase. This further complication of cooling histories should be addressed in future work.

To conclude, transient models with various timings and amounts of increase in exhumation rates give a good fit to the observed thermochronometric cooling ages in the Olympic Mountains. However, there are also other factors that are not included in our modeling approach, but that can explain the still observed mismatch between modeled ages and sample ages. First, the increase in rates (which is interpreted as the impact of glaciers) seems to be spatially (and temporally) variable. Second, the shape of the exhumation rate pattern could be different from the assumed perfect ellipse shape and explain some of the excluded, 'outlier' samples (e.g. samples OP1521 and OP1582), too. A possible reduction in topography, e.g. due to Pleistocene glaciation (Ehlers et al., 2006), was also not included in the model. And the exhumation history could be even more complicated, where exhumation rates increase or decrease additionally to the imposed 2 – 3 Ma.

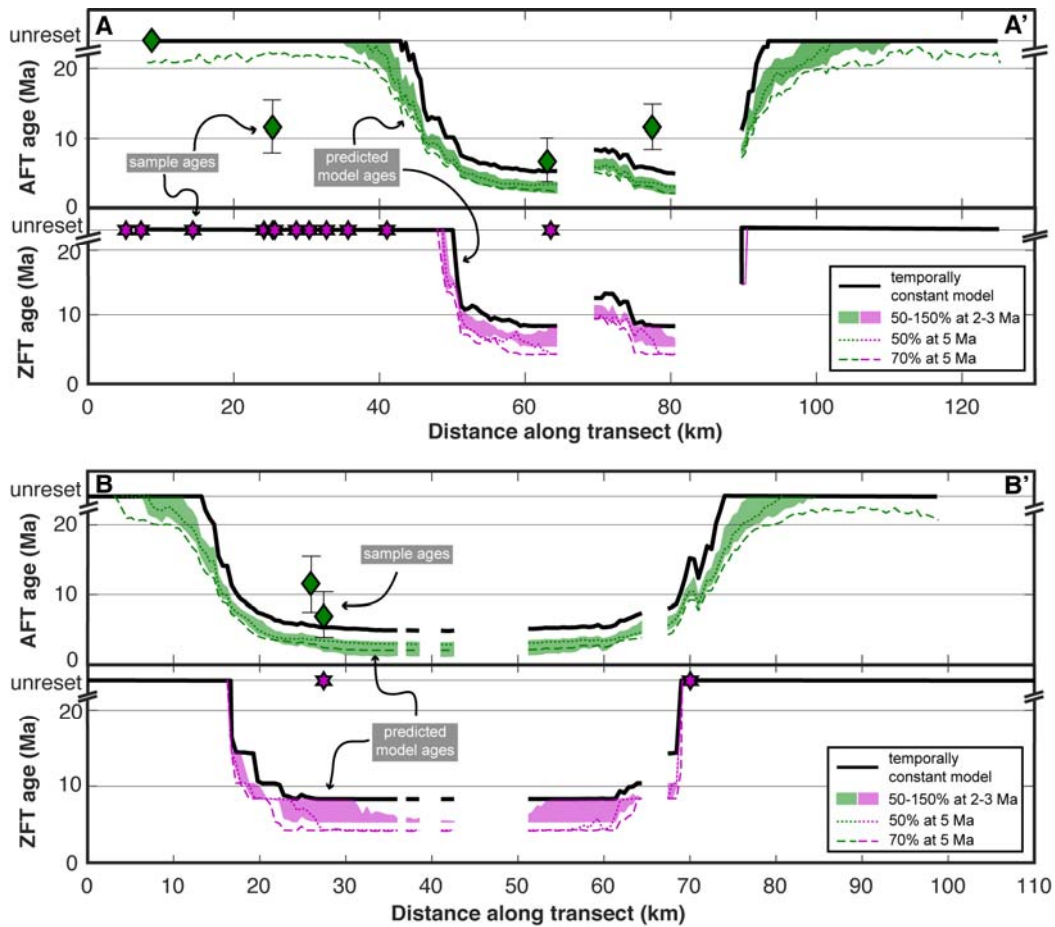


Figure DR9: Literature AFT/ZFT ages (symbols) and modeled AFT/ZFT ages along the swath profiles A-A' and B-B'. Literature data are taken from an elevation interval between 0 and 600 m asl, to make the analysis comparable to our own equal elevation data. Model ages are taken from an elevation interval between 200 – 500 m. For location of the swaths see Figure 1b, AHe/ZHe ages together with elevation/precipitation can be found in Figure 2. Note: only fully reset or unreset literature samples are considered.

DR3.3 Horizontal velocity models

In a previous study the horizontal velocity component additional to the vertical velocity component was considered in a modeling approach as well (Batt et al., 2001). For this model, a cross section through the accretionary wedge is assumed, starting at the offshore deformation front and extending to the east coast of the Olympic Peninsula. Sedimentary material derived from the subducting slab can enter the accretionary wedge either via frontal accretion or underplating. Batt et al. (2001) concluded that ~90% of the sediment needs to be frontally accreted (and hence a high horizontal velocity component is required) in order to explain their observed age pattern of AHe, AFT and ZFT.

However, there are several reasons why we believe that the contribution of horizontal velocities in the Olympics is less important than previously suggested. First the approach of Batt et al. (2001) is questionable. They base their model on a predefined erosion rate function, which governs the vertical velocity field (and hence

the rock uplift). Although the rates of the function are variable from model to model run (in order to explore the best-fitting rates), the shape of the function stays constant. This erosion rate function is determined from uplifted river terraces at the west coast (Pazzaglia and Brandon, 2001) and long-term exhumation rates from inversion of AFT ages (Brandon et al., 1998). These AFT-derived exhumation rates are based on a 1D thermo-kinematic model, but do not consider the proposed effect of horizontal velocities (e.g. the protracted cooling history due to longer travel paths) or possible changes of rates with time. So simply based on the shape of the function, highest erosion rates are always observed 20 – 30 km from the western coastline. Due to the fact that this corresponds also to the area of high horizontal velocities (generally speaking the horizontal velocities decrease from west to east), a strong interplay between horizontal and vertical velocities can always be expected for these models.

Second, the equation stated for the vertical velocity in Batt et al. (2001) contains a mistake, because their derivative of the horizontal velocity is not correct (it is missing a $\eta v_c h_0$ term). Although a full derivation of horizontal and vertical velocities is beyond the scope of this paper (see e.g. Batt et al., 2001; Pazzaglia and Brandon, 2001), we reformulate the corrected equation for the vertical velocity component,

$$w(x, z) = \alpha \left(\dot{\varepsilon}(x) - \frac{z \dot{\varepsilon}(x)}{h(x)} - z \cdot \tan \phi \cdot \left(\frac{\eta v_c h_0 - \int_0^x \dot{\varepsilon}(x)}{h^2(x)} \right) \right) + (1 - \alpha) \dot{\varepsilon}(x)$$

where the vertical velocity $w(x,z)$ at place x and z in the wedge is calculated based on the erosion rate at the surface $\dot{\varepsilon}(x)$, thickness of the wedge $h(x)$, angle of subduction ϕ , the incoming sediment material (product of sediment porosity η , subduction velocity v_c and sediment thickness h_0). The factor α is the ratio between frontal accretion and sedimentary underplating (so if $\alpha=1$ all sediment is frontally accreted). The formula for the horizontal velocity in Batt et al. (2001) is correct,

$$u(x) = \alpha \left(\frac{\eta v_c h_0 - \int_0^x \dot{\varepsilon}(x)}{h(x)} \right)$$

with the underlying assumption that horizontal velocities do not vary with depth but only in x -direction. Examining this equation shows that the horizontal velocity is highest for 100% frontal accretion ($\alpha=1$) and zero, if only underplating occurs ($\alpha=0$).

Using these two equations and the values given in table DR6, we also perform model runs in Pecube with both horizontal and vertical velocities. However, these model runs are highly simplified compared to our model runs described in chapter DR3.2: they neither include topography, nor do they consider an increase in rates at 2 – 10 Ma. Furthermore, the model follows a cross section across the Olympic Peninsula parallel to the subduction direction (with a bearing of 54° , for the trace of the cross section see Figure DR4). We derive the integral of the erosion rate by integrating over our preferred elliptic exhumation rate pattern (from the constant rate model run) along the cross section. Using the derived integral and the values listed in table DR6, we calculate the horizontal and vertical velocities along the cross section with a matlab script (using the above equations) and put these values back in Pecube. The resulting pattern of ages is depicted in Figure DR10. A high α -value (i.e. high horizontal velocities) generates AHe and ZHe ages that are too old compared to the observed ages, because it basically shifts the area of reset ages further to the east. For the $\alpha=0$ model run sample ages are often younger than the model ages

(particularly on the west side), which is probably related to the increase in rates at around 2 – 3 Ma due to Pleistocene glaciation. We did not include this increase in our horizontal model runs.

All the points mentioned above lead us to the conclusion, that for our chosen exhumation rate pattern a high horizontal velocity (meaning a high amount of frontal accretion) is not necessary to explain the observed age pattern in the Olympic Mountains for the AHe and ZHe thermochronometer systems we consider. This is also in accordance with seismic studies showing that sedimentary underplating is taking place in the Olympics (Calvert et al., 2011). Hence, our approach to model an increase in exhumation rates at Plio-Pleistocene time using a model that only considers vertical movement seems to be viable. However, we acknowledge the possibility that horizontal motion may be significant for higher temperature thermochronometers (e.g. ZFT) that integrate over longer time scales and distances.

Table DR 6: Additional list of parameters used for the horizontal velocity runs.

Parameter	Value	Source
incoming sediment thickness	2.5 km	approximate value offshore from the Olympic Peninsula (Booth-Rea et al., 2008)
subduction velocity	34 km/Ma	calculated plate velocity of the down going Juan de Fuca plate at the latitude of the Olympics (Dobrovine and Tarduno, 2008)
sediment porosity	27 %	taken from Batt et al. (2001)
angle of subduction	10°	average value of the present day angle of subduction for the Cascadia subduction zone at the latitude of the Olympics (Davis and Hyndman, 1989)

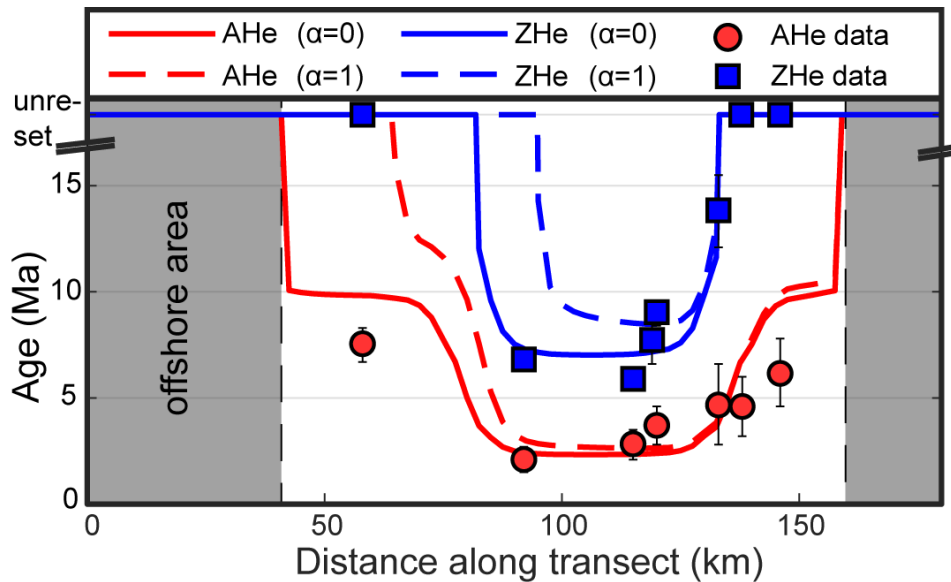


Figure DR10: Modeled and observed AHe and ZHe ages from 2D kinematic model simulations extracted along a profile across the Olympic Peninsula (see Fig. DR4 for location). Note that in offshore regions no exhumation is defined within the model, hence all ages are unreset. The α -value corresponds to the amount of material that is frontally accreted in the wedge ($\alpha=1$, 100% frontal accretion with maximum horizontal velocity; $\alpha=0$, 100% underplating with no horizontal velocity). A large horizontal velocity component predicts anomalously old cooling ages for both AHe and ZHe.

REFERENCES

- Adam, J., Klaeschen, D., Kukowski, N., and Flueh, E., 2004, Upward delamination of Cascadia Basin sediment infill with landward frontal accretion thrusting caused by rapid glacial age material flux: *Tectonics*, v. 23, doi: 10.1029/2002TC001475.
- Adams, B.A., and Ehlers, T.A., 2017, Deciphering topographic signals of glaciation and rock uplift in an active orogen: a case study from the Olympic Mountains, USA: *Earth Surface Processes and Landforms*, doi: 10.1002/esp.4120.
- Adams, B.A., Hodges, K.V., Whipple, K.X., Ehlers, T.A., van Soest, M.C., and Wartho, J., 2015, Constraints on the tectonic and landscape evolution of the Bhutan Himalaya from thermochronometry: Late Cenozoic Evolution of Bhutan: *Tectonics*, v. 34, p. 1329–1347, doi: 10.1002/2015TC003853.
- Batt, G.E., Brandon, M.T., Farley, K.A., and Roden-Tice, M., 2001, Tectonic synthesis of the Olympic Mountains segment of the Cascadia wedge, using two-dimensional thermal and kinematic modeling of thermochronological ages: *Journal of Geophysical Research: Solid Earth*, v. 106, p. 26731–26746, doi: 10.1029/2001JB000288.
- Berger, A.L., Gulick, S.P.S., Spotila, J.A., Upton, P., Jaeger, J.M., Chapman, J.B., Worthington, L.A., Pavlis, T.L., Ridgway, K.D., Willems, B.A., and McAleer,

- R.J., 2008, Quaternary tectonic response to intensified glacial erosion in an orogenic wedge: *Nature Geoscience*, v. 1, p. 793–799, doi: 10.1038/ngeo334.
- Booth-Rea, G., Klaeschen, D., Grevemeyer, I., and Reston, T., 2008, Heterogeneous deformation in the Cascadia convergent margin and its relation to thermal gradient (Washington, NW USA): *Tectonics*, v. 27, doi: 10.1029/2007TC002209.
- Brandon, M.T., Roden-Tice, M.K., and Garver, J.I., 1998, Late Cenozoic exhumation of the Cascadia accretionary wedge in the Olympic Mountains, northwest Washington State: *Geological Society of America Bulletin*, v. 110, p. 985–1009, doi: 10.1130/0016-7606(1998)110<0985:LCEOTC>2.3.CO;2.
- Brandon, M.T., and Vance, J.A., 1992, Tectonic evolution of the Cenozoic Olympic subduction complex, Washington State, as deduced from fission track ages for detrital zircons: *American Journal of Science*, v. 292, p. 565–636, doi: 10.2475/ajs.292.8.565.
- Calvert, A.J., Preston, L.A., and Farahbod, A.M., 2011, Sedimentary underplating at the Cascadia mantle-wedge corner revealed by seismic imaging: *Nature Geoscience*, v. 4, p. 545–548, doi: 10.1038/ngeo1195.
- Clague, J.J., 1989, Quaternary Geology of the Canadian Cordillera, *in* Fulton, R.J. ed., *Quaternary Geology of Canada and Greenland*, Ottawa, Geological Survey of Canada, *Geology of Canada* 1, p. 17–96.
- Crosson, R.S., and Owens, T.J., 1987, Slab geometry of the Cascadia Subduction Zone beneath Washington from earthquake hypocenters and teleseismic converted waves: *Geophysical Research Letters*, v. 14, p. 824–827, doi: 10.1029/GL014i008p00824.
- Davis, E.E., and Hyndman, R.D., 1989, Accretion and recent deformation of sediments along the northern Cascadia subduction zone: *Geological Society of America Bulletin*, v. 101, p. 1465–1480.
- Dobrovine, P.V., and Tarduno, J.A., 2008, A revised kinematic model for the relative motion between Pacific oceanic plates and North America since the Late Cretaceous: *Journal of Geophysical Research*, v. 113, doi: 10.1029/2008JB005585.
- Easterbrook, D.J., 1986, Stratigraphy and chronology of quaternary deposits of the Puget Lowland and Olympic Mountains of Washington and the Cascade Mountains of Washington and Oregon: *Quaternary Science Reviews*, v. 5, p. 145–159, doi: 10.1016/0277-3791(86)90180-0.
- Eddy, M.P., Clark, K.P., and Polenz, M., 2017, Age and volcanic stratigraphy of the Eocene Siletzia oceanic plateau in Washington and on Vancouver Island: *Lithosphere*, v. 9, p. 652–664, doi: 10.1130/L650.1.
- Ehlers, T.A., Farley, K.A., Rusmore, M.E., and Woodsworth, G.J., 2006, Apatite (U-Th)/He signal of large-magnitude accelerated glacial erosion, southwest British Columbia: *Geology*, v. 34, p. 765–768.

- Farley, K.A., 2002, (U-Th)/He Dating: Techniques, Calibrations, and Applications: *Reviews in Mineralogy and Geochemistry*, v. 47, p. 819–844, doi: 10.2138/rmg.2002.47.18.
- Glotzbach, C., van der Beek, P., Carcaillet, J., and Delunel, R., 2013, Deciphering the driving forces of erosion rates on millennial to million-year timescales in glacially impacted landscapes: An example from the Western Alps: *Journal of Geophysical Research: Earth Surface*, v. 118, p. 1491–1515, doi: 10.1002/jgrf.20107.
- Haug, G.H., Ganopolski, A., Sigman, D.M., Rosell-Mele, A., and others, 2005, North Pacific seasonality and the glaciation of North America 2.7 million years ago: *Nature*, v. 433, p. 821.
- Hayes, G.P., Wald, D.J., and Johnson, R.L., 2012, Slab1.0: A three-dimensional model of global subduction zone geometries: SLAB1.0 3D SUBDUCTION GEOMETRY: *Journal of Geophysical Research: Solid Earth*, v. 117, p. n/a-n/a, doi: 10.1029/2011JB008524.
- Herman, F., Seward, D., Valla, P.G., Carter, A., Kohn, B., Willett, S.D., and Ehlers, T.A., 2013, Worldwide acceleration of mountain erosion under a cooling climate: *Nature*, v. 504, p. 423–426, doi: 10.1038/nature12877.
- Hourigan, J.K., Reiners, P.W., and Brandon, M.T., 2005, U-Th zonation-dependent alpha-ejection in (U-Th)/He chronometry: *Geochimica et Cosmochimica Acta*, v. 69, p. 3349–3365, doi: 10.1016/j.gca.2005.01.024.
- Hyndman, R.D., and Wang, K., 1993, Thermal constraints on the zone of major thrust earthquake failure: The Cascadia Subduction Zone: *Journal of Geophysical Research: Solid Earth*, v. 98, p. 2039–2060, doi: 10.1029/92JB02279.
- Hyndman, R.D., Yorath, C.J., Clowes, R.M., and Davis, E.E., 1990, The northern Cascadia subduction zone at Vancouver Island: Seismic structure and tectonic history: *Canadian Journal of Earth Sciences*, v. 27, p. 313–329.
- Lewis, T.J., and Bentkowski, W.H., 1988, Potassium, Uranium and Thorium Concentrations of Crustal Rocks: a Data File: Geological Survey of Canada, Open File, 1–165 p.
- Lewis, T.J., Bentkowski, W.H., Davis, E.E., Hyndman, R.D., Souther, J.G., and Wright, J.A., 1988, Subduction of the Juan de Fuca Plate: Thermal consequences: *Journal of Geophysical Research: Solid Earth*, v. 93, p. 15207–15225, doi: 10.1029/JB093iB12p15207.
- McCrorry, P.A., Blair, J.L., Waldhauser, F., and Oppenheimer, D.H., 2012, Juan de Fuca slab geometry and its relation to Wadati-Benioff zone seismicity: JDF SLAB GEOMETRY AND WBZ SEISMICITY: *Journal of Geophysical Research: Solid Earth*, v. 117, p. n/a-n/a, doi: 10.1029/2012JB009407.
- McQuarrie, N., and Ehlers, T.A., 2015, Influence of thrust belt geometry and shortening rate on thermochronometer cooling ages: Insights from thermokinematic and erosion modeling of the Bhutan Himalaya: *GEOMETRY, RATES, AND MODELED COOLING AGES: Tectonics*, v. 34, p. 1055–1079, doi: 10.1002/2014TC003783.

- Meesters, A.G.C.A., and Dunai, T.J., 2005, A noniterative solution of the (U-Th)/He age equation: *Geochemistry, Geophysics, Geosystems*, v. 6, doi: 10.1029/2004GC000834.
- Montgomery, D.R., 2002, Valley formation by fluvial and glacial erosion: *Geology*, v. 30, p. 1047–1050, doi: 10.1130/0091-7613(2002)030<1047:VFBFAG>2.0.CO;2.
- Montgomery, D.R., and Greenberg, H.M., 2000, Local relief and the height of Mount Olympus: *Earth Surface Processes and Landforms*, v. 25, p. 385–396.
- Pazzaglia, F.J., and Brandon, M.T., 2001, A fluvial record of long-term steady-state uplift and erosion across the Cascadia forearc high, western Washington State: *American Journal of Science*, v. 301, p. 385–431.
- Phillips, B.A., Kerr, A.C., Mullen, E.K., and Weis, D., 2017, Oceanic mafic magmatism in the Siletz terrane, NW North America: Fragments of an Eocene oceanic plateau? *Lithos*, v. 274–275, p. 291–303, doi: 10.1016/j.lithos.2017.01.005.
- Porter, S.C., 1964, Composite Pleistocene snow line of Olympic Mountains and Cascade Range, Washington: *Geological Society of America Bulletin*, v. 75, p. 477–482.
- Shuster, D.L., Ehlers, T.A., Rusmoren, M.E., and Farley, K.A., 2005, Rapid Glacial Erosion at 1.8 Ma Revealed by 4He/3He Thermochronometry: *Science*, v. 310, p. 1668–1670, doi: 10.1126/science.1118519.
- Stewart, R.J., and Brandon, M.T., 2004, Detrital-zircon fission-track ages for the “Hoh Formation”: implications for late Cenozoic evolution of the Cascadia subduction wedge: *Geological Society of America Bulletin*, v. 116, p. 60–75.
- Stübner, K., Drost, K., Schoenberg, R., Böhme, M., Starke, J., and Ehlers, T.A., 2016, Asynchronous timing of extension and basin formation in the South Rhodope core complex, SW Bulgaria, and northern Greece: *Tectonics*, v. 35, p. 136–159, doi: 10.1002/2015TC004044.
- Tabor, R.W., and Cady, W.M., 1978, The structure of the Olympic Mountains, Washington: Analysis of a subduction zone: *US Govt. Print. Off.*, v. 1033.
- Thackray, G.D., 2001, Extensive Early and Middle Wisconsin Glaciation on the Western Olympic Peninsula, Washington, and the Variability of Pacific Moisture Delivery to the Northwestern United States: *Quaternary Research*, v. 55, p. 257–270, doi: 10.1006/qres.2001.2220.
- Underwood, M.B., Hoke, K.D., Fisher, A.T., Davis, E.E., Giambalvo, E., Zuhlsdorff, L., and Spinelli, G.A., 2005, Provenance, Stratigraphic Architecture, and Hydrogeologic Influence of Turbidites on the Mid-Ocean Ridge Flank of Northwestern Cascadia Basin, Pacific Ocean: *Journal of Sedimentary Research*, v. 75, p. 149–164, doi: 10.2110/jsr.2005.012.
- Vermeesch, P., 2010, HelioPlot, and the treatment of overdispersed (U–Th–Sm)/He data: *Chemical Geology*, v. 271, p. 108–111, doi: 10.1016/j.chemgeo.2010.01.002.

Whipp, D.M., Ehlers, T.A., Braun, J., and Spath, C.D., 2009, Effects of exhumation kinematics and topographic evolution on detrital thermochronometer data: *Journal of Geophysical Research*, v. 114, doi: 10.1029/2008JF001195.